



HAL
open science

Mechanobiologically induced bone-like nodules: Matrix characterization from micro to nanoscale

Hassan Rammal, Marie Dubus, Nicolas B Bercu, Eric Mathieu, Christine Terryn, Michaël Molinari, Sophie Lemarié Gangloff, Nadine Nassif, Cédric Mauprivez, Fabienne Quilès, et al.

► To cite this version:

Hassan Rammal, Marie Dubus, Nicolas B Bercu, Eric Mathieu, Christine Terryn, et al.. Mechanobiologically induced bone-like nodules: Matrix characterization from micro to nanoscale. *Nanomedicine: Nanotechnology, Biology and Medicine*, 2020, 29, pp.102256. 10.1016/j.nano.2020.102256 . hal-02909596

HAL Id: hal-02909596

<https://hal.science/hal-02909596>

Submitted on 24 Aug 2020

HAL is a multi-disciplinary open access archive for the deposit and dissemination of scientific research documents, whether they are published or not. The documents may come from teaching and research institutions in France or abroad, or from public or private research centers.

L'archive ouverte pluridisciplinaire **HAL**, est destinée au dépôt et à la diffusion de documents scientifiques de niveau recherche, publiés ou non, émanant des établissements d'enseignement et de recherche français ou étrangers, des laboratoires publics ou privés.

Mechanobiologically induced bone-like nodules: Matrix characterization from micro to nanoscale

Hassan Rammal, PhD^{a,b}, Marie Dubus, PhD^{a,b}, Nicolas B Bercu, PhD^c, Eric Mathieu, MSc^d,
Christine Terryn, PhD^e, Michaël Molinari, PhD^{c,f}, Sophie C. Gangloff, PhD^{a,g},
Nadine Nassif, PhD^h, Cédric Mauprivez, PhD, MD^{a,b,i}, Fabienne Quilès, PhD^{j*,1}, Halima
Kerdjoudj, PhD^{a,b,**,1}

^a Université de Reims Champagne Ardenne, BIOS EA 4691, Reims, France

^b Université de Reims Champagne Ardenne, UFR d'Odontologie, Reims, France

^c Université de Reims Champagne Ardenne, LRN EA 4682, Reims, France

^d Institut National de la Santé et de la Recherche Médicale, UMR-S 1121, Strasbourg Cedex,
France

^e Université de Reims Champagne Ardenne, PICT, Reims, France

^f Université de Bordeaux, CBMN UMR CNRS5248, IPB Bordeaux, Pessac, France

^g Université de Reims Champagne Ardenne, UFR de Pharmacie, Reims, France

^h CNRS, Sorbonne Université, Collège de France, Laboratoire Chimie de la Matière Condensée
de Paris (LCMCP), Paris, France

ⁱ Pôle Médecine bucco-dentaire, Centre Hospitalier Universitaire de Reims, France

^j Université de Lorraine, CNRS, LCPME, Nancy, France

Disclosure statement: Authors declare no competing personal or financial competing interest. All other authors have nothing to disclose.

Availability of data and materials: All data generated or analyzed during this study are included in this published article [and its supplementary information files]. If not, they are available from the corresponding author on reasonable request.

Funding: This research did not receive any specific grant from funding agencies in the public, commercial, or not-for-profit sectors.

*Correspondence to: F. Quilès, LCPME, UMR-CNRS 7564, Laboratoire de Chimie Physique et Microbiologie pour les Matériaux et l'Environnement, Villers-lès-Nancy, France.

**Correspondence to: H. Kerdjoudj, EA 4691, Biomateriaux et Inflammation en Site Osseux, Pôle Santé, UFR d'Odontologie, SFR-CAP Santé (FED 4231), URCA, Reims, France.

E-mail addresses: fabienne.quiles@univ-lorraine.fr, (F. Quilès), halima.kerdjoudj@univ-reims.fr. (H. Kerdjoudj).

¹ Both authors have contributed equally to this work.

Received 16 April 2020; revised 15 June 2020; accepted 19 June 2020

Abstract

In bone tissue engineering, stem cells are known to form inhomogeneous bone-like nodules on a micrometric scale. Herein, micro- and nano-infrared (IR) micro-spectroscopies were used to decipher the chemical composition of the bone-like nodule. Histological and immunohistochemical analyses revealed a cohesive tissue with bone-markers positive cells surrounded by dense mineralized type-I collagen. Micro-IR gathered complementary information indicating a non-mature collagen at the top and periphery and a mature collagen within the nodule. Atomic force microscopy combined to IR (AFM-IR) analyses showed distinct spectra of “cell” and “collagen” rich areas. In contrast to the “cell” area, spectra of “collagen” area revealed the presence of carbohydrate moieties of collagen and/or the presence of glycoproteins. However, it was not possible to determine the collagen maturity, due to strong bands overlapping and/or possible protein orientation effects. Such findings could help developing protocols to allow a reliable characterization of in vitro generated complex bone tissues.

Key words:

Nano/micro scale; Differentiated stem cells; Bone-like nodule; Infrared microscopy; AFM-IR spectroscopy

Introduction

Tissue engineering and regenerative medicine have emerged as a potential solution to overcome the shortcomings of autologous tissue transplants and/or organ donors. To this end, the implementation of various concurrent processes is required, including the recruitment and differentiation of cells to form complex tissues in a spatially organized manner. Among these tissues, bone has a remarkably well organized structure in which the quantity, the quality, and the distribution of its different components (i.e. type I collagen (COL-I) fibrils and calcium phosphates nanocrystals) are associated with the mechanical properties of the tissue. In vitro, bone regeneration events are described through the culture of mesenchymal stem cells that form three-dimensional bone-like nodules. These structures are highly textured composites of submicrometric inorganic wispy needle-like crystals embedded within an organic extracellular matrix (ECM) and are also spatially inhomogeneous on a micrometric scale in terms of physical morphology (i.e. collagen fibrils, microvesicles, cells) and chemical content (i.e. minerals).¹⁻⁵ Collagen fibrils, with a mean diameter of 78 nm, assemble into a highly organized and close-packed lamellar structure.⁶ Mineralization occurs in the COL-I-based ECM where the nucleation takes place in gap regions but also on the fibril surface. Gap regions are nano-scaled structures, of about 40 nm long and 20 nm high, created by a unique arrangement of COL-I molecules⁶ where the crystals grow through their c-axes within the fibrils parallel to the COL-I axis. The nature and organization of the collagenous fibrillar network are critical for bone physiology,⁷ where sparse and disorganized fibrils result in inadequate bone mineralization.^{8,9} Although considerable breakthroughs have been achieved over the past 30 years, resulting in a wealth of knowledge in many fields (i.e. biochemistry, cell biology, and molecular biology), the systematic characterization of bone-like nodules at the submicrometric scale is barely described in the literature.

Infrared spectroscopy (IR) has emerged as a powerful method to analyze complex connective tissues, using fresh or fixed and embedded specimens. Infrared spectra provide valuable information about the chemical identification, the structure analysis, and the dynamic and molecular conformations. IR spectral analysis determines changes in cortical and trabecular bone quality as it provides simultaneously quantitative and qualitative information on all main bone tissue components in a spatially resolved manner (i.e. 5-40 μm , mostly depending on the light source and the type of detector).^{10,11} Infrared microscopy ($\mu\text{-IR}$) was successfully applied to

characterize the mineralization of tissues,^{12,13} and stem cells or osteoblasts differentiation state¹⁴⁻¹⁷ by assessing mineral-to-matrix ratio, carbonate-to-phosphate ratio, and the crystallinity and collagen cross-link maturity, providing a qualitative information on the ECM compounds and maturation.^{18,19} However, the spatial inhomogeneous features of bone-like nodules constrain the IR spatial resolution. Recently, efforts have been made to circumvent these constraints by coupling atomic force microscopy with infrared spectroscopy (AFM-IR).²⁰ This technique measures the transient thermal vibration of an AFM probe in contact with a sample, induced by the sample absorbing the light from a tunable infrared laser. With a lower spatial resolution, AFM-IR extends IR functionality to include spectroscopic mapping at the nanometer length scale, typically in the order of 50-100 nm.²¹⁻²³

Advances in material sciences have garnered interest in providing intrinsic material features, such as composition, mechanical properties and surface topography; allowing stem cells commitment into desired phenotype.²⁴ Inorganic/organic materials (ioM) with special component assemblies are thought to be useful to guide the bone regeneration process.²⁵ We recently developed a bioactive and osteoinductive material made of poorly crystalline carbonated hydroxyapatite, dicalcium phosphate dihydrate and chitosan and hyaluronic acid with mechanical and structural features required for bone regeneration.²⁶ Herein, both IR and AFM-IR tools were combined in order to obtain precise information on the chemical composition of individual bone-like nodules formed on ioM at the micro- and nanoscales. In short, the gathered data support the potential use of μ -IR and AFM-IR as reliable tools for ECM characterization of in vitro generated complex bone organoid tissues.

Results and discussion

Inorganic/organic material (ioM) made of poorly crystalline carbonated hydroxyapatite, dicalcium phosphate dihydrate and chitosan/hyaluronic acid biopolymers has been recently shown to boost the early stem cell differentiation, upon one week of culture, into osteoblast-like lineage through mechanobiological phenomena.²⁶ Despite the early expression of osteocalcin (OCN), known to impair bone formation, we observed the formation of a visible refringent material over four weeks of culture.²⁷ Starting from two weeks of culture on ioM, stem cells formed aggregates, (see videos in supplementary data) which constantly increased in size, reaching ≈ 0.4 mm² and 115

μm in height with a density of around 9 ± 2 nodules in a 15.6 mm (in diameter) culture well at the fourth week (Figures 1, A and SI-1). Histological transversal sections of nodules revealed a cohesive tissue with randomly distributed cells embedded within a collagen-rich matrix and continuous cell layers at the periphery (Figure 1, B and C). Immunohistochemistry assessment revealed the presence of positive cells for OCN and osteopontin (OPN) but also for dentin matrix acidic phosphoprotein-1 (DMP-1), an osteocyte marker (Figure 1, D). Transmission electron and atomic force microscopies showed dense bundles and fibrils surrounding cells, characterized by 67 and 62 nm banding periodicity with fibril diameter of around 175 nm (Figure 1, E and F), signature of COL-I.^{28,29} Furthermore, Alizarin red staining evidenced a mineral deposit (Figure 1, G). Taken together, these results suggest that cell aggregation leads to the formation of bone-like nodule structures. Standard molecular technics such as qRT-PCR are typically used to assess the in vitro osteoblastic commitment and are commonly combined with immunofluorescent or histological matrix staining including Von Kossa, Alizarin red or Sirius red.³⁰ However, such approaches require considerable sample preparation, are semi-quantitative and, crucially, fail to provide sufficient information to define a specific mineralization stage of a cell-compact nodule.³

COL-I, the most abundant protein in bone, confers to bone its mechanical stability, strength and toughness. An altered hierarchical structure of collagen molecules affects the mineralization process that occurs within and around fibers.^{8,9,31} Herein, bone-like nodules were characterized at different scales using single scan polarization-resolved second harmonic generation (SS-pSHG) and polarized light (PLM) microscopies. The nonlinear signal being sensitive to the polarization state of the excitation light, SS-pSHG emission is likely to depend on the optical anisotropy that results from the collagen molecular organization.³² Indeed, collagen fibrils are efficient generators for SS-pSHG due to their well-ordered structure; three-polypeptide chains wind together to form a triple helix that further self-assembles periodically into collagen fibrils. Only non-centrosymmetric and fibrillar COL-I structures, in contrast to immature and cytoplasmic COL-I, are able to generate SS-pSHG signal following multiphoton microscopy imaging.^{33,34} Strong SS-pSHG signals within nodules as well as thin alternating bright and dark structures were noticed, suggesting a highly ordered molecular arrangement (Figure 2, A). To go further on the collagen organization, observations were made using PLM, allowing the observation down to the microscale of birefringent COL-I. Interestingly, thin alternating bright and dark bands were observed locally within bone-like nodules (Figure 2, B) and were surrounded by micrometric and birefringent

crystals reminding the morphology of dicalcium phosphate dihydrate from the ioM substrate. After a 45° rotation of the polarizers, extinction of the light occurred in areas where collagen molecules lie down parallel to the direction of the polarizers, indicating a twisted plywood organization (i.e. cholesteric) of collagen fibrils (Figure 2, C and D). Notice that the birefringent texture (Figure 2, E) was not due to folds of the histological section that might occur when placed on the glass slide. Plywood geometry was further confirmed by using a quartz first order retardation plate (Figure 2, F) displaying blue and yellow interference colors, depending on the orientation of the collagen fibrils. Such pattern is described in osteons of human compact bone³⁵ and in collagen/apatite bone-like matrix.³⁶

Infrared spectroscopic imaging has been used to describe changes in bone as functions of age, disease, fracture, and osteoporosis treatment.¹¹ Infrared microscopy (μ -IR) was already used to examine sections of bone, providing spatially detailed information relative to mineral and organic composition.¹¹⁻¹³ μ -IR was performed on 28 days-old air-dried bone-like nodules, avoiding interferences in the spectra due to the chosen method of fixation.³⁷ Recorded spectra in transmission mode highlighted differences in the spectral IR fingerprint from the periphery and the central areas (Figure 3, A). Band wavenumbers were determined by the calculation of the second derivative spectra (Figure SI-2) and their assignments are gathered in Table 1.³⁸⁻⁴³ In the 1000-1160 cm^{-1} region, PO_4 stretching, a feature of hydroxyapatite, was clearly observed at the nodule periphery (Figure 3, Aa and Ad, Table 1). In this mode, the infrared beam crosses the whole sample, including the substrate. Thus, the detected inorganic phosphate could be assigned to the ioM substrate.²⁶ The central area of the nodule revealed additional bands assigned to polysaccharide compounds (1161; 1155; 1116; 1108 and 1048 cm^{-1}) and nucleic acids (1090 cm^{-1} , Figure 3, Ab and Ac). For bands mainly assigned to proteins (1700-1500 cm^{-1}), the spectral features were also different from the center to the periphery areas of the nodule, especially for the amide-I band, known to be sensitive to the protein conformation. While the nodule periphery showed the simplest amide bands profile (Figure 3, Aa and Ad), the shape of amide-I bands, resulting from the central area, showed a different distribution of individual amide bands (Figure 3, Ab and Ac). Amide-I bands at the periphery were poorly resolved and centered close to 1650 cm^{-1} , showing mostly proteins with random coils and/or α -helices and few proteins with β -sheets (Figures 3, Aa and Ad, SI-3, Table 1). The small shoulder observed at 1687 cm^{-1} suggests the occurrence of a small amount of collagen. The amide-I band close to 1660 cm^{-1} , associated with the one close to 1690

cm^{-1} in mature collagen, was not resolved^{38,41} (Figure SI-3, A and D). Clearly resolved collagen amide-I bands (at 1685- and 1660 cm^{-1} , Figure SI-3, B and C) of the central area indicate the presence of a more mature collagen. These results are consistent with Ghita et al, who analyzed the spatial distribution of the mature bone matrix showing nodule central parts with higher maturation degree along with crystalline hydroxyapatite, whereas immature ECM was dominant at the edges of bone-like nodules.⁴⁴ The presence of polysaccharide bands, between 1160 and 1000 cm^{-1} (Figure 3, Ab and Ac), suggests the occurrence of carbohydrate moieties from collagen with also the possible presence of glycoproteins and/or proteoglycans, such as OCN.⁴⁵ Regardless of the area, β -sheets structures were observed at ~ 1635 - 1637 cm^{-1} and 1516 - 1521 cm^{-1} , whereas β -turns can be suggested from the shoulder at 1678 cm^{-1} . The proportion of collagen was also calculated from the ratio $\{1660 + 1690\}/\text{amide-I}$, and the results showed a ratio of ~ 0.1 in the peripheral areas of the nodule (Figures 3, Aa and Ad, SI-3a and SI-3d) and ~ 0.6 from the spectra recorded in more central areas (Figures 3, Ab and Ac, SI-3b and SI-3c). These data indicate that there was a higher quantity of collagen in the central areas. Ratio of integrated intensities for the bands at ~ 1660 and ~ 1690 cm^{-1} ($1660/1690$), called “collagen maturity”, indicated changes in secondary structure of collagen in relation with the mineralization process.⁴⁶ The collagen band at ~ 1660 cm^{-1} was not resolved in the spectra from the peripheral areas of the nodule, signature of an immature collagen (Figure SI-3a and SI-3d). The ratios calculated from the spectra of the nodule central areas varied from 0.9 to 1.5 (Figure SI-3b and SI-3c, respectively). These disparities are probably in direct relationship with the higher amount of collagen in the nodule's central areas with respect to the peripheral areas. Other ratios, as “mineral maturity” (ratio 1030/1110) or “mineralization index” (ratio 1184-910/1712-1592)⁴⁶ were not calculated because of the non-negligible contribution of the phosphate species from the ioM substrate.

To overcome the undesirable contribution of the ioM substrate, spectra were recorded in reflection mode on the same nodule/area, showing different general profiles with the absence of the phosphate fingerprint (i.e. around 1030 cm^{-1} for the most intense band, Figure 3, B). This could be explained by the fact that in this mode, the nodule is not entirely crossed by the infrared beam and that the resulting information comes mainly from the upper side of the nodule. The amide-I and -II bands, mainly observed at 1692-1695 cm^{-1} and 1558-1568 cm^{-1} , respectively, were assigned to collagen. Amide-I and amide-II bands at 1675-1681 cm^{-1} and 1521-1524 cm^{-1} were attributed to proteins with β -turn conformation and β -structures, respectively (Figure 3, Be and Bf).

Band at 1660-1665 cm^{-1} , usually assigned to 3-turn helix component from collagen, was correlated to pre-osteoblast differentiation into osteoblasts.⁴¹ Herein, this band was only resolved in the spectrum of the central area (Figures 3 Bf and SI-3f), confirming the presence of collagen with a very low maturity stage in the peripheral areas (Figure 3, Be and Bg). With calculated ratios $\{1660 + 1690\}/\text{amide-I}$ of about 0.4, 0.6, and 0.3 (Figure SI-3e, SI-3f and SI-3g, respectively), the proportion of collagen was higher in the center area of the nodule, strengthening the above conclusion. The value of 1660/1690 ratio was about 0.4 (Figure SI-3f). Taken together and compared to the above results recorded in the transmission mode, these results confirm the presence of immature collagen at the top of the nodule. Amide-I bands were accompanied by bands at 1747 and 1721-1723 cm^{-1} that are assigned mostly to C=O stretching modes of esters and carboxylic acids, respectively. These bands, either associated with phospholipids and proteins, were more intense in our study than usually seen in spectra of cells. This can be attributed to the occurrence of matrix vesicle membranes involved in bone mineralization.^{3,47} Amide-II band, observed as a shoulder at 1610 cm^{-1} , was assigned to side-chain groups of collagen, where arginine, glutamic and aspartic acids collagen residues absorption occurs.⁴⁸⁻⁵⁰ The occurrence of a large amount of collagen was also confirmed by the presence of its specific amide III band at 1341-1343 cm^{-1} .⁴³ $\mu\text{-IR}$ in transmission and reflection modes gathered complementary information, showing a non-mature collagen at the top and the periphery of the nodule and an overall more mature collagen within the bone-like nodule. Indeed, during osteoblastic differentiation, multi-layered osteoblasts are thought to deposit an immature nodule matrix through their basal pole,³ in full agreement with our observations.

One of the main limitations of conventional $\mu\text{-IR}$ being the spatial resolution, an innovative approach using atomic force microscope coupled with infrared spectroscopy (AFM-IR) was used to provide chemical information with a spatial resolution of ≥ 50 nm.²⁰ By placing the AFM probe on an identified region, it is then possible to acquire a localized IR spectrum at a spatial resolution of a few tens of nm. This technique is currently used for the nanoscale analysis of anisotropic materials, including large molecules and proteins. Owing to possible nonlinearities in energy absorption across samples of different thickness, AFM-IR spectra were recorded on histological 5 μm sections placed on a transparent and total internal reflective surface (i.e., zinc selenide). Spectra of the “cell rich” or “collagen rich” areas in the 28-day-old nodule, identified through HES staining, were recorded (Figure 4). Band wavenumbers

were determined by the calculation of the second derivative spectra (Figure SI-4), and band assignments are gathered in Table 2.^{38-41,43,51} The high intensity of the amide I band with respect to the rest of the fingerprint region matched AFM-IR spectra of pure collagen fibrils,⁵² suggesting a high specific orientation of proteins present within analyzed areas.⁵³ Spectra of the “cell-rich” area showed an important variety of features in amide-I region (1700-1600 cm^{-1}), suggesting a high diversity in proteins and conformations. Spectral fingerprints of collagen (1696, 1664 and 1606 cm^{-1}), proteins with β -turn (1678 and 1631 cm^{-1}) and α /random (1645 cm^{-1}) conformations occurred in majority, but in different proportions (Figure 4, A). In addition, significant proportions of proteins with β -sheets conformation (1614, 1515 and 1623 cm^{-1}) and β -turn (1676 cm^{-1}), assigned to cellular proteins, were also observed. Band assigned to C=O stretching from esters at $\sim 1738 \text{ cm}^{-1}$ was high in spectra of Figure 4, Aa and Ab, suggesting the occurrence of phospholipids (along with the presence of the PO₂ symmetric stretching at $\sim 1250 \text{ cm}^{-1}$) from the cellular membranes. In the spectrum from the “cell-rich” area (Figure 4, Ac), the intensity of the bands at $\sim 1736 \text{ cm}^{-1}$ assigned to C=O stretching of phospholipid esters from the cellular membrane and the amide-I band below 1650 cm^{-1} had the lowest relative intensities (Figure 4, Ac). The most intense band here was observed at 1664 cm^{-1} and assigned to collagen, showing the close contact of cells with collagen fibrils (Figure 1, E). Spectra of the “collagen-rich” area revealed highly overlapped amide-I bands leading to a very broad and poorly resolved group of bands, as it was already observed for pure collagen.⁵² However, owing to the second derivative spectra, we were able to identify collagen, proteins with β -turn/ β -sheet and α /random structures. The occurrence of a significant amount of phospholipids can be suggested from bands at ~ 1742 and $\sim 1255 \text{ cm}^{-1}$ (Figure 4, B, Table 2). In contrast to “cell-rich” area, spectra showed additional weak intensity bands in region 1000-1150 cm^{-1} assigned to polysaccharides. These latter suggest a signature from carbohydrate moieties of collagen⁴³ and/or the presence of glycoproteins. Considering the strong overlapping of bands and the possible polarization effects of AFM-IR in both areas (i.e. “cell-rich” and “collagen-rich”), we were not able to determine unambiguously ratios 1660/1690 cm^{-1} and further collagen maturation.

General comments

In summary, spatially resolved spectra were recorded with μ -IR and AFM-IR techniques on bone-like nodules. They provided a reliable characterization of their chemical content, marked by prominent signatures from collagen, proteins with β -turn/ β -sheet and α /random structures, phospholipids and polysaccharides. Depending on the analyzed areas (i.e. periphery vs central areas and “cell-rich” vs “collagen-rich” areas), we noticed strong differences in spectral profiles. Such discrepancy can be attributed to the heterogeneous cell repartition within the ECM but also to the ECM components’ contribution including their chemical composition, molecule orientation/conformation, maturation degree etc. (Tables 1 and 2). Herein, COL-I fibrils were evidenced as the major component of the nodule. The amide-I band, typically observed in the 1600-1700 cm^{-1} range, is the most intense absorption band in collagen and is directly related to the backbone conformation. SS-pSHG and PLM showed the presence of a matured COL-I, which was partially confirmed by infrared spectroscopy investigations as 1660/1690 cm^{-1} ratios depend on the localization in the nodule, and they were lower than those calculated for bone specimens (i.e. ~ 2).^{12,13,38,46} Using FTIR spectroscopy, 1660/1690 cm^{-1} ratio was shown to be proportional to the relative amounts of the trivalent cross-link pyridinoline and the divalent (immature) crosslink dihydroxylysinoxaline.⁵⁴ The intermolecular crosslinking offers to the fibrillar collagen mechanical properties such as tensile strength and viscoelasticity. Constant ECM remodeling is expected to introduce changes in their supra organizational properties, influencing this ratio.⁵⁵ Notably, the marked presence of metalloproteinase in our bone-like nodules forming cells media could be a signature of ECM remodeling (data not shown). Although Gourion-Arsiquaud et al reported that the 1660/1690 cm^{-1} ratio determined by AFM-IR indicates the collagen maturity,²³ this point could be discussed. Indeed, crystallinity and orientation in the sample probed by AFM-IR systems using polarized light could influence relative IR peak intensities. SS-pSHG and PLM microscopies indicated highly ordered and oriented collagen fibers within the nodule. Thus, the undesirable effect of polarization cannot be ignored. In bone, N-linked glycoproteins such as DMP-1 and BSP bind to COL-I and initiate conformational changes from random coil to β -sheet structures that are able to sequester Ca^{2+} ions.⁵⁶ Owing to its flexible random coil and β -turn structures, OPN is in contrast considered as a potent inhibitor of mineralization caused by the production of an electrostatic repulsion of inorganic phosphate ions.⁵⁶ Through its γ -carboxyglutamic acid (Gla) residues, OCN, the most abundant non-collagenous protein found in bone, binds to calcium and exhibits a compact calcium dependent α -helical conformation,

promoting the fixation of hydroxyapatite crystals to the bone matrix. Note that vibrational spectroscopic analysis of proteoglycans and glycosaminoglycans is not discriminant between different species. Regarding the importance of β -sheet, β -turn and α -helical structures in bone mineralization, the following band ratios were calculated: (a) β -turn structures/amide-I, (b) β -sheet structures/amide-I, (c) α -helix structures + random coil structures/amide-I. The obtained results did not allow highlighting meaningful differences between the analyzed areas whatever the spectral resolution.

Lipids are described as nucleators for collagen fibrils mineralization in vitro and they are also part of the matrix vesicle membranes in bone mineralization.^{3,47} The occurrence of the high amount of phospholipids was likely attributed to matrix vesicles. Most reports state that successful osteoblast commitment occurs when the produced ECM is positive to Alizarin red or von Kossa staining. Despite the positive staining (Figure 2, D and E), ultrastructural and spectroscopy investigations did not show the presence of minerals. Conclusions drawn from Alizarin red are probably not related to bone minerals (hydroxyapatite) but to dystrophic minerals resulting from culture media or necrotic cells, known to promote inappropriate mineralization.^{57,58} Finally, we recently reported that chromatin condensation was highly correlated with the state of differentiation with less condensed chromatin organization in stem cell nuclei compared to localized hypercondensed chromatin in differentiated cell nuclei.²⁶ Thus, the absence of important vibrational signal of nuclei acids could be attributed to the hypercondensed region in cell within the nodule, as condensed DNA is known to decrease IR absorbance.^{59,60}

Experimental

Stem cell culture

Human umbilical cord harvesting was approved ethically and methodologically by our local Research Institution and was conducted with informed patients (written consent) in accordance with the usual ethical legal regulations (Article R 1243-57). All procedures were done in accordance with our authorization and registration number DC-2014-2262 given by the National “Cellule de Bioéthique”. Wharton's jelly stem cells (WJ-SCs), enzymatically isolated, were amplified at density of 3×10^3 cell/cm² in α -MEM culture medium supplemented with 10% decomplemented fetal bovine serum (FBS), 1% Penicillin/Streptomycin/Amphotericin B and 1%

Glutamax® (v/v, Gibco) and maintained in a humidified atmosphere of 5% CO₂ at 37 °C with a medium change every two days. At the fourth passage, WJ-SCs were seeded in 24-well plates at 24×10^3 cells/cm² on UV-decontaminated inorganic/organic material (ioM)²⁶ and glass coverslip, and maintained in culture for four weeks.

Scanning electron and digital microscopy

After four weeks of culture, WJ-SCs were fixed with 2.5% (w/v) glutaraldehyde (Sigma Aldrich) at room temperature for 1 h. Samples were dehydrated in graded ethanol solutions from 50 to 100% and desiccated in hexamethyldisilazane (Sigma Aldrich) for 10 min. After air-drying at room temperature, samples were sputtered with a thin gold–palladium film under a JEOL ion sputter JFC 1100 and viewed (at 500× magnification) using a field emission gun-scanning electron microscope (FEG-SEM) (JEOL, JSM-7900F) and with a digital microscope (Keyence, VHX-6000). FEG-SEM images were acquired from secondary electrons at primary beam energy between 5 to 20 kV.

Histological analysis

Cytoplasmic, nuclear and extracellular matrix features within bone-like nodules were followed by histology. After four weeks of culture, resulting bone-like nodules were fixed in 1% (w/v) paraformaldehyde for one hour and dehydrated in solutions with gradually increasing concentration of ethanol content, using a Shandon Excelsior Tissue Processor (Thermo Fisher Scientific, Waltham, MA, USA). Five-micrometer thick sections were performed on paraffin-embedded bone-like nodules (rotation microtome AP280, Leica Microsystems). Hematoxylin–eosin–safran (HES), Masson's Trichrome, Alcian blue, Alizarin red and Von Kossa stainings were performed separately on consecutive tissue sections and on various tissue zone sections and images (at 40× magnification) were taken using a scanner iScan Coreo AU (Roche Ò Ventana).

DMP1, OCN and OPN immunolabeling

Paraffin embedded bone-like nodule sections were incubated overnight with rabbit polyclonal antibodies targeting OPN, OCN and DMP1 (at a 1/100 dilution in blocking buffer, Calbiochem). After DPBS multiple rinse, secondary goat anti-rabbit IgG biotinylated antibodies (Invitrogen) were used at a 1/100 dilution for 30 min at room temperature followed by Alexa 488-conjugated streptavidin at 1/2000 dilution (Invitrogen) for 30 min at room temperature. Nuclei were counter-

stained with DAPI. The stained sections were mounted and imaged by laser scanning microscopy (Zeiss LSM 710 NLO, 20× objective).

Transmission electron microscopy

After four weeks of culture, WJ-SCs were rinsed with cacodylate buffer solution (125 mM), fixed in 2% paraformaldehyde and 2.5% glutaraldehyde in 50 mM cacodylate buffer at pH 7.4 for 2 h at room temperature and finally post-fixed in 1% osmium tetroxide in 125 mM cacodylate buffer for 30 min. Samples were dehydrated in solutions with gradually increasing concentration of ethanol for 15 min. Samples were then embedded in epoxy resin (48.2% epon 812, 34% anhydride nadic methyl, 16.4% anhydride [2-dodeceny] succinic, and 1.5% 2,4,6-tris dimethylaminoethyl phenol) for 48 h at 60 °C. After resin polymerization, a thermic shock in liquid nitrogen was first performed to remove the substrate. To obtain transversal sections of embedded samples, the cutting surface was reoriented by preparing a small block using a circular saw (Bronwill Scientific) and sticking them on new ones. Ultra-thin cross sections (100 nm in thickness) were performed using an automatic ultra-microtome (Ultracut-E Ultramicrotome, Reichert Jung). The specimen was observed with a transmission electron microscope EM208 (FEI Company, Philips) operating with an accelerating voltage of 70 kV. Images were captured on SO163 Kodak films.

Atomic force microscopy

A Multimode-8 AFM setup from Bruker (Santa Barbara, USA) using PeakForce tapping mode in air was used in order to obtain high quality topographical images. Such an operational mode is capable to control the tip-sample interaction forces with high accuracy, therefore significantly improving the AFM image quality compared to the standard intermittent contact AFM modes. Scanning rates of 0.5 to 1 Hz were used with a constant actuation frequency of 1 kHz; all AFM images were acquired with a resolution of 512×512 data points. Silicon Scan Asyst-Air triangular AFM probes from Bruker (Santa Barbara, USA) with ultra-sharp tips (nominal tip radius of curvature of 2 nm, nominal spring constant of 0.4 N/m, and nominal resonance frequency of 70 kHz) were used in order to minimize non-desirable tip-sample broadening effects and to allow high resolution topographical AFM measurements.

Single scan polarization-resolved second harmonic generation imaging

SS-pSHG images were obtained with a confocal microscope (LSM 710-NLO, Carl Zeiss SAS, Germany) coupled with CHAMELEON femtosecond Titanium-Sapphire Laser (Coherent, USA). Laser polarization was changed on circular by adding a $\lambda/4$ waveplate on light path. Paraffin embedded bone-like nodule sections were excited at 860 nm and SHG signal was collected through a 20 \times objective (ON: 0.8).

Polarized light microscopy

Observations were performed on unstained paraffin embedded bone-like nodule sections using a transmission Zeiss Axio Imager A2 POL. The microscope was equipped with the standard accessories for examination of birefringent samples under polarized light (i.e. crossed polars and a quartz first order retardation plate) and an Axio Cam CCD camera.

Infrared microspectroscopy (μ -IR)

Spectra of air-dried samples were recorded between 4000 and 800 cm^{-1} on a Bruker Vertex 70 v spectrometer equipped with a Hyperion 2000 microscope and a $\times 15$ objective controlled by the OPUS 7.5 software. A KBr beam splitter and an MCT detector were used. The resolution of the single beam spectra was 4 cm^{-1} . Spectra of bone-like nodules were recorded in transmission and reflection modes. Masks of 40 \times 40 and 80 \times 80 μm were used to record the transmission and reflectance spectra, respectively. The sizes of the masks were chosen to get enough energy at the detector in order to record reliable spectra with good signal-to-noise ratios. The number of bidirectional double-sided interferogram scans was 64 and 128, respectively, which corresponded to a 60 and 120 s accumulation, respectively. All interferograms were Fourier-processed using the power phase correction and a Blackman-Harris three-term apodization function. Measurements were performed at 21 ± 1 $^{\circ}\text{C}$ in an air-conditioned room. Water vapor subtraction was performed when necessary, and the baseline was corrected at 3800, 2500, 1900 and 900 cm^{-1} before further analysis of the spectra. The second derivative spectra were used to determine the number and position of the bands in region 1750-1500 cm^{-1} for the subsequent spectral curve fitting with Gaussian curves.

Atomic force microscopy combined to infrared spectroscopy (AFM-IR)

Measurements on sections of paraffin-embedded nodules were performed using a NanoIR2 microscope (Bruker, Santa Barbara, CA, USA) at ambient temperature in a spectral range of 1800-900 cm^{-1} with a spectral resolution of 4 cm^{-1} . The IR laser source used for these measurements was an OPO laser (EKSPLA, Vilnius, Lithuania) with 12 ns long pulses and a repetition rate of 10 Hz. The NanoIR2 system allowed to perform AFM-IR combined measurements using IR pulsed beam²⁰ which was aligned with the position of the AFM probe on the sample surface. The AFM was operated in contact mode; the topography images were obtained using EX-C450-AN cantilevers (Bruker, Santa Barbara, CA, USA). While the system was operated in contact mode, the cantilever deflection oscillates with an amplitude which is proportional to the absorption coefficient of the sample²⁰ corresponding to the pulsed laser wavelength. Samples were placed on ZnSe sampling flats for NanoIR2. Prior to analysis, the spectrum of paraffin recorded separately was removed by spectral subtraction (Figure SI-5). Subsequent to AFM-IR data acquisition and in order to distinguish the “cell-rich” area from the “collagen-rich” area, bone-like nodule tissue sections were stained with HES using standard procedures (please refer to histological analysis section) and imaged at 40 × magnification.

Acknowledgment

The authors are grateful to the staff of Reims Maternity Hospital for providing umbilical cords and the staff of the Core PICT (URCA) for SS-pSHG and FEG-SEM imaging. The authors thank Yoann Boulatika (Keyence, France) for his technical help with the digital microscopy, Caroline Fichel and Nicole Bouland for their precious effort with histological analysis, and Pr. Pierre Schaaf and Dr. Fouzia Boulmedais from INSERM U1121 and ICS (Université de Strasbourg, France) for the “spray coating of interacting species” (SSCIS) setup. We also thank Mrs. M. Cantener (English teacher from Odontology faculty of Reims) for the careful reading of the manuscript.

Appendix A. Supplementary data

Supplementary data to this article can be found online at

<https://doi.org/10.1016/j.nano.2020.102256>.

References

1. Hall BK, Miyake T. All for one and one for all: condensations and the initiation of skeletal development. *BioEssays News Rev Mol Cell Dev Biol* 2000;22:138-47.
2. Lian JB, Stein GS. Concepts of osteoblast growth and differentiation: basis for modulation of bone cell development and tissue formation. *Crit Rev Oral Biol Med Off Publ Am Assoc Oral Biol* 1992;3:269-305.
3. Mechiche Alami S, Gangloff SC, Laurent-Maquin D, Wang Y, Kerdjoudj H. Concise review: in vitro formation of bone-like nodules sheds light on the application of stem cells for bone regeneration. *Stem Cells Transl Med* 2016;5:1587-93.
4. Gentleman E, Swain RJ, Evans ND, Boonrungsiman S, Jell G, Ball MD, et al. Comparative materials differences revealed in engineered bone as a function of cell-specific differentiation. *Nat Mater* 2009;8:763-70.
5. Owen TA, Aronow M, Shalhoub V, Barone LM, Wilming L, Tassinari MS, et al. Progressive development of the rat osteoblast phenotype in vitro: reciprocal relationships in expression of genes associated with osteoblast proliferation and differentiation during formation of the bone extracellular matrix. *J Cell Physiol* 1990;143:420-30.
6. Orgel JPRO, Irving TC, Miller A, Wess TJ. Microfibrillar structure of type I collagen in situ. *Proc Natl Acad Sci* 2006;103:9001-5.
7. Landis WJ. The strength of a calcified tissue depends in part on the molecular structure and organization of its constituent mineral crystals in their organic matrix. *Bone* 1995;16:533-44.
8. Khajuria DK, Soliman M, Elfar JC, Lewis GS, Abraham T, Kamal F, et al. Aberrant structure of fibrillar collagen and elevated levels of advanced glycation end products typify delayed fracture healing in the diet-induced obesity mouse model. *Bone* 2020;137:115436.
9. Misof K, Landis WJ, Klaushofer K, Fratzl P. Collagen from the osteogenesis imperfecta mouse model (oim) shows reduced resistance against tensile stress. *J Clin Invest* 1997;100:40-5.
10. Naumann D. FT-infrared and FT-Raman spectroscopy in biomedical research. *Appl Spectrosc Rev* 2001;36:239-98.
11. Paschalis EP, Gamsjaeger S, Klaushofer K. Vibrational spectroscopic techniques to assess bone quality. *Osteoporos Int* 2017;28:2275-91.
12. Boskey AL, Mendelsohn R. Infrared spectroscopic characterization of mineralized tissues. *Vib Spectrosc* 2005;38:107-14.

13. Boskey A, Pleshko Camacho N. FT-IR imaging of native and tissue engineered bone and cartilage. *Biomaterials* 2007;28:2465-78.
14. Krafft C, Salzer R, Seitz S, Ern C, Schieker M. Differentiation of individual human mesenchymal stem cells probed by FTIR microscopic imaging. *Analyst* 2007;132:647-53.
15. Ami D, Neri T, Natalello A, Mereghetti P, Doglia SM, Zanoni M, et al. Embryonic stem cell differentiation studied by FT-IR spectroscopy. *Biochim Biophys Acta* 2008;1783:98-106.
16. Faillace ME, Phipps RJ, Miller LM. Fourier transform infrared imaging as a tool to chemically and spatially characterize matrix-mineral deposition in osteoblasts. *Calcif Tissue Int* 2013;92:50-8.
17. Chonanant C, Bambery KR, Jearanaikoon N, Chio-Srichan S, Limpaboon T, Tobin M, et al. Discrimination of micromass-induced chondrocytes from human mesenchymal stem cells by focal plane array-Fourier transform infrared microspectroscopy. *Talanta* 2014;130:39-48.
18. Khanna R, Katti KS, Katti DR. Bone nodules on chitosan polygalacturonic acid-hydroxyapatite nanocomposite films mimic hierarchy of natural bone. *Acta Biomater* 2011;7:1173-83.
19. Addison WN, Nelea V, Chicatun F, Chien YC, Tran-Khanh N, Buschmann MD, et al. Extracellular matrix mineralization in murine MC3T3-E1 osteoblast cultures: an ultrastructural, compositional and comparative analysis with mouse bone. *Bone* 2015;71:244-56.
20. Dazzi A, Prater CB, Hu Q, Chase DB, Rabolt JF, Marcott C. AFM-IR: combining atomic force microscopy and infrared spectroscopy for nanoscale chemical characterization. *Appl Spectrosc* 2012;66:1365-84.
21. Amarie S, Zaslansky P, Kajihara Y, Griesshaber E, Schmahl WW, Keilmann F. Nano-FTIR chemical mapping of minerals in biological materials. *Beilstein J Nanotechnol* 2012;3:312-23.
22. Imbert L, Gourion-Arsiquaud S, Villarreal-Ramirez E, Spevak L, Taleb H, van der Meulen MCH, et al. Dynamic structure and composition of bone investigated by nanoscale infrared spectroscopy. *PloS One* 2018;13e0202833.
23. Gourion-Arsiquaud S, Marcott C, Hu Q, Boskey AL. Studying variations in bone composition at nano-scale resolution: a preliminary report. *Calcif Tissue Int* 2014;95:413-8.
24. Murphy WL, McDevitt TC, Engler AJ. Materials as stem cell regulators. *Nat Mater* 2014;6:547-57.
25. Stevens MM. Biomaterials for bone tissue engineering. *Mater Today* 2008;11:18-25.

26. Rammal H, Dubus M, Aubert L, Reffuveille F, Laurent-Maquin D, Terryn C, et al. Bioinspired nanostructured substrates: suitable environment for bone regeneration. *ACS Appl Mater Interfaces* 2017;9:12791-801.
27. Rammal H, Entz L, Dubus M, Moniot A, Bercu NB, Sergheraert J, et al. Osteoinductive material to fine-tune paracrine crosstalk of mesenchymal stem cells with endothelial cells and osteoblasts. *Front Bioeng Biotechnol* 2019;7:256.
28. Li T, Chang SW, Rodriguez-Florez N, Buehler MJ, Shefelbine S, Dao M, et al. Studies of chain substitution caused sub-fibril level differences in stiffness and ultrastructure of wildtype and oim/oim collagen fibers using multifrequency-AFM and molecular modeling. *Biomaterials* 2016;107:15-22.
29. Asgari M, Latifi N, Heris HK, Vali H, Mongeau L. In vitro fibrillogenesis of tropocollagen type III in collagen type I affects its relative fibrillar topology and mechanics. *Sci Rep* 2017;7:1392.
30. Iwaniec UT, Wronski TJ, Turner RT. Histological analysis of bone. *Methods Mol Biol* 2008;447:325-41.
31. Gautieri A, Uzel S, Vesentini S, Redaelli A, Buehler MJ. Molecular and mesoscale mechanisms of osteogenesis imperfecta disease in collagen fibrils. *Biophys J* 2009;97:857-65.
32. Thomas B, McIntosh D, Fildes T, Smith L, Hargrave F, Islam M, et al. Second-harmonic generation imaging of collagen in ancient bone. *Bone Rep* 2017;7:137-44.
33. Green NH, Delaine-Smith RM, Askew HJ, Byers R, Reilly GC, Matcher SJ. A new mode of contrast in biological second harmonic generation microscopy. *Sci Rep* 2017;7:13331.
34. Chen X, Nadiarynkh O, Plotnikov S, Campagnola PJ. Second harmonic generation microscopy for quantitative analysis of collagen fibrillar structure. *Nat Protoc* 2012;87:654-69.
35. Giraud-Guille MM. Liquid crystalline order of biopolymers in cuticles and bones. *Microsc Res Tech* 1994;27:420-8.
36. Nassif N, Gobeaux F, Seto J, Belamie E, Davidson P, Panine P, et al. Self-assembled collagen-apatite matrix with bone-like hierarchy. *Chem Mater* 2012;22:3307-9.
37. Zohdi V, Whelan DR, Wood BR, Pearson JT, Bamberg KR, Black MJ. Importance of tissue preparation methods in FTIR micro-spectroscopical analysis of biological tissues: « traps for new users ». *PloS One* 2015;10:e0116491.

38. Paschalis EP, Verdellis K, Doty SB, Boskey AL, Mendelsohn R, Yamauchi M. Spectroscopic characterization of collagen cross-links in bone. *J Bone Miner Res Off J Am Soc Bone Miner Res* 2001;16:1821-8.
39. Kong J, Yu S. Fourier transform infrared spectroscopic analysis of protein secondary structures. *Acta Biochim Biophys* 2007;39:549-59.
40. Nagant C, Pitts B, Nazmi K, Vandenbranden M, Bolscher JG, Stewart PS, et al. Identification of peptides derived from the human antimicrobial peptide LL-37 active against biofilms formed by *Pseudomonas aeruginosa* using a library of truncated fragments. *Antimicrob Agents Chemother* 2012;56:5698-708.
41. Giorgini E, Conti C, Ferraris P, Sabbatini S, Tosi G, Centonze M, et al. FT-IR microscopic analysis on human dental pulp stem cells. *Vib Spectrosc* 2011;57:30-4.
42. Karampas IA, Kontoyannis CG. Characterization of calcium phosphates mixtures. *Vib Spectrosc* 2013;64:126-33.
43. Petibois C, Gousspillou G, Wehbe K, Delage JP, Déléris G. Analysis of type I and IV collagens by FT-IR spectroscopy and imaging for a molecular investigation of skeletal muscle connective tissue. *Anal Bioanal Chem* 2006;386:1961-6.
44. Ghita A, Pascut FC, Sottile V, Notingher I. Monitoring the mineralisation of bone nodules in vitro by space- and time-resolved Raman microspectroscopy. *Analyst* 2014;139:55-8.
45. Mizuguchi M, Fujisawa R, Nara M, Nitta K, Kawano K. Fourier transform infrared spectroscopic study of Ca²⁺-binding to osteocalcin. *Calcif Tissue Int* 2001;69:337-42.
46. Farlay D, Duclos ME, Gineyts E, Bertholon C, Viguet-Carrin S, Nallala J, et al. The ratio 1660/1690 cm⁽⁻¹⁾ measured by infrared microspectroscopy is not specific of enzymatic collagen cross-links in bone tissue. *PloS One* 2011;6:e28736.
47. Thouverey C, Strzelecka-Kiliszek A, Balcerzak M, Buchet R, Pikula S. Matrix vesicles originate from apical membrane microvilli of mineralizing osteoblast-like Saos-2 cells. *J Cell Biochem* 2009;106:127-38.
48. Eastoe JE. The amino acid composition of mammalian collagen and gelatin. *Biochem J* 1995;61:589-600.
49. Gauza-Włodarczyk M, Kubisz L, Włodarczyk D. Amino acid composition in determination of collagen origin and assessment of physical factors effects. *Int J Biol Macromol* 2017;104:987-91.

50. Chirgadze YN, Fedorov OV, Trushina NP. Estimation of amino acid residue side-chain absorption in the infrared spectra of protein solutions in heavy water. *Biopolymers* 1975;14:679-94.
51. Ruggeri FS, Longo G, Faggiano S, Lipiec E, Pastore A, Dietler G. Infrared nanospectroscopy characterization of oligomeric and fibrillar aggregates during amyloid formation. *Nat Commun* 2015;6:7831.
52. Kulik AJ, Simone Ruggeri F, Gruszecki W, Dietler G. Nanoscale infrared spectroscopy of light harvesting proteins, amyloid structures and collagen fibres. *Microsc Anal* 2014;28:11-5.
53. Amenabar I, Poly S, Nuansing W, Hubrich EH, Govyadinov AA, Huth F, et al. Structural analysis and mapping of individual protein complexes by infrared nanospectroscopy. *Nat Commun* 2013;4:2890.
54. de Campos Vidal B, Mello MLS. Collagen type I amide I band infrared spectroscopy. *Micron* 2011;42:283-9.
55. Mandair GS, Morris MD. Contributions of Raman spectroscopy to the understanding of bone strength. *BoneKEy Rep* 2015;4:620.
56. George A, Veis A. (2008). Phosphorylated proteins and control over apatite nucleation, crystal growth, and inhibition. *Chem Rev* 2008;108:4670-93.
57. Boonrungsiman S, Gentleman E, Carzaniga R, Evans ND, McComb DW, Porter AE, et al. The role of intracellular calcium phosphate in osteoblast-mediated bone apatite formation. *Proc Natl Acad Sci* 2012;109:14170-5.
58. Mechiche Alami S, Rammal H, Boulagnon-Rombi C, Velard F, Lazar F, Drevet R, et al. Harnessing Wharton's jelly stem cell differentiation into bone-like nodule on calcium phosphate substrate without osteoinductive factors. *Acta Biomater* 2017;49:575-89.
59. Zelig U, Kapelushnik J, Moreh R, Mordechai S, Nathan I. Diagnosis of cell death by means of infrared spectroscopy. *Biophys J* 2009;97:2107-14.
60. Matthäus C, Boydston-White S, Miljković M, Romeo M, Diem M. Raman and infrared microspectral imaging of mitotic cells. *Appl Spectrosc* 2006;60:1-8.

Figure caption:

Figure 1: Bone-like nodule characterization. (A) Field emission gun-scanning electron microscopy (FEG-SEM, scale bar = 100 μm), (B) hematoxylin eosin saffron (HES) staining, showing nuclei (blue) and cells (pink) multilayered at the surface and randomly distributed within fibrous tissues and (C) Masson's Trichrome staining, showing nuclei (brown), cytoplasm (dark) and collagen (green) (scale bar: 100 μm). (D) Immunostaining (green) and nuclei (blue) revealing the expression of osteocalcin (OCN), osteopontin (OPN) and dentine matrix protein (DMP-1) (Scale bars: 16 μm). (E) Transmission electron microscopy (TEM, magnification $\times 8000$), (F) atomic force microscopy (AFM), showing the presence of type I collagen within the nodule (F₁: d-spacing of ~ 67 nm and F₂: fibril diameter of ~ 175 nm), (G) Alizarin red staining showing mineral deposit within the nodule (scale bars: 100 μm).

Figure 2: Collagen signature. (A) Single scan polarized-resolved Second Harmonic Generation (SS-pSHG, scale bar: 100 μm) and (B-D) polarized light microscopy (scale bars: 100 and 20 μm), revealing highly ordered collagen fibrils within the nodule. The band * appears bright and dark depending upon the polarizers rotation from 0-90° (C) to 45-135° (D). ** indicating the surrounding paraffin. E: sample without polarizers. F: image after inducing a first order retardation with a gamma plate with polarizers at 0-90°.

Figure 3: Micro-infrared spectra of a nodule. (A) in transmission mode (mask: 40 $\mu\text{m} \times 40 \mu\text{m}$). (B) in reflection mode (mask: 80 $\mu\text{m} \times 80 \mu\text{m}$). Inserts: optical representation of analyzed regions (Scale bars: 100 μm). Offsets of spectra are used for clarity (a, b, c and d spectra correspond to blue, red, black, and pink squares in figure A while e, f and g spectra correspond to green, black and blue squares in figure B), respectively.

Figure 4: AFM-infrared spectra of a nodule. (A) cell-rich area. (B) collagen-rich area. Inserts: HES stained bone-like nodule slices with green spots corresponding to analyzed areas. Scale bars: 100 μm .

Table 1: Assignments of principal infrared vibrational bands of the 1800–900 cm^{-1} region of the μ -IR spectrum of the nodule (Key: v: stretching, δ : bending, a: antisymmetric, s: symmetric).

Table 2: Assignments of principal infrared vibrational bands of the 1800–900 cm^{-1} region of the AFM-IR spectrum of the nodule (Key: sh: shoulder, v: stretching, δ : bending, a: antisymmetric, s: symmetric).

Figure 1:

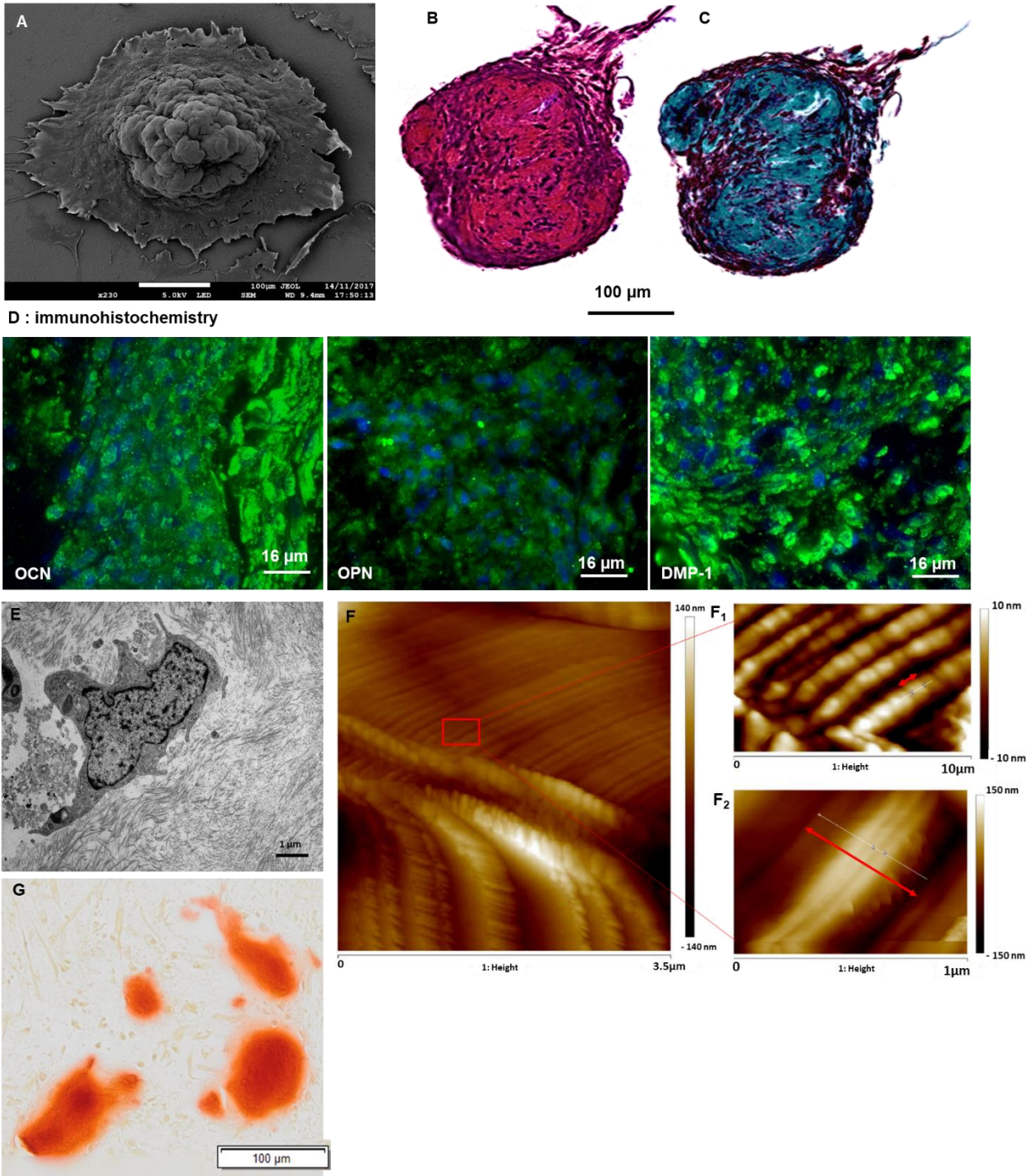


Figure 2:

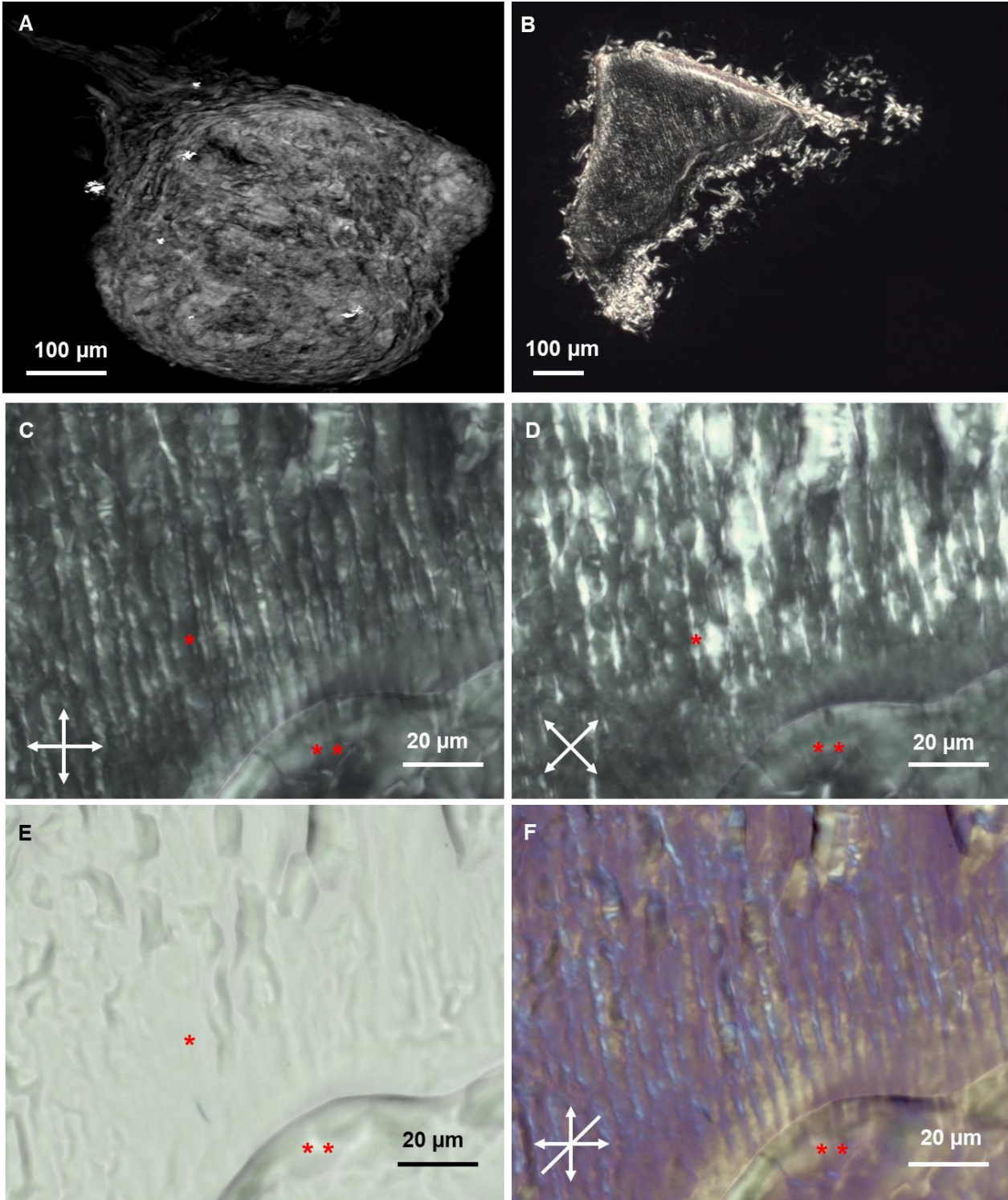


Figure 3:

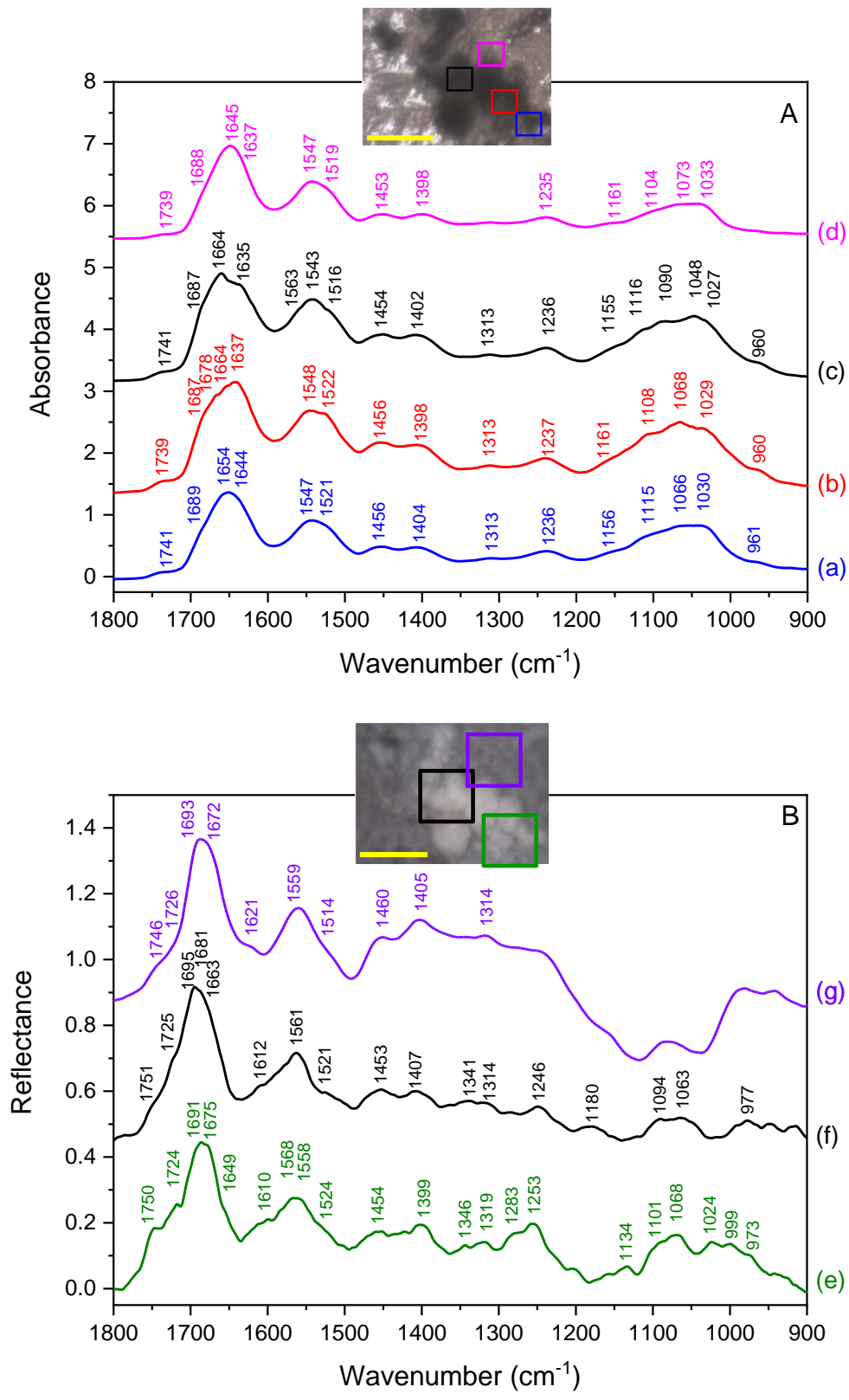


Figure 4:

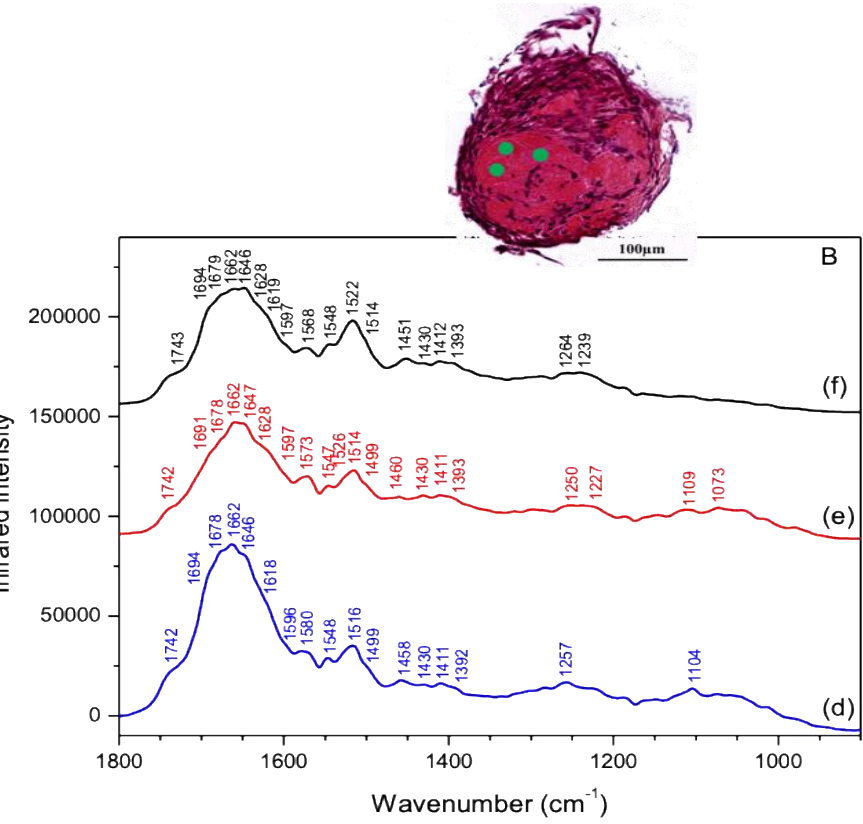
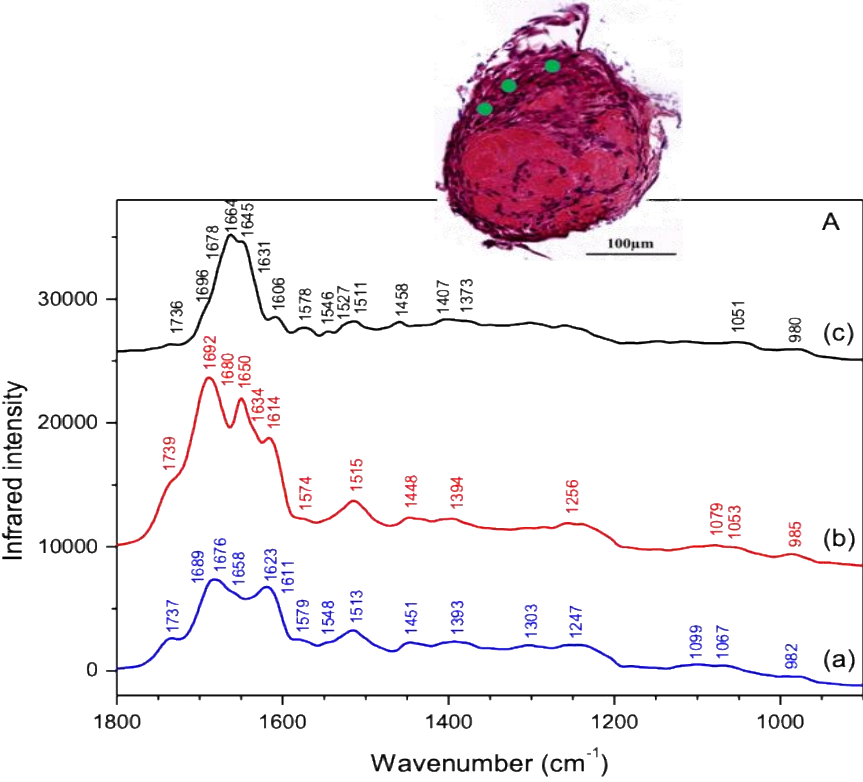


Table 1:

Transmission mode				Reflection mode			Tentative assignment
1A _a	1A _b	1A _c	1A _d	1B _e	1B _f	1B _g	
1741	1739	1740	1741	1750	1750	1746	vC=O (esters, phospholipids)
1723	1724	1722	1720	1724	1724	1725	vC=O (carboxylic acids)
1689	1687	1687	1687	1692	1694	1693	Amide-I, collagen
	1678			1675	1681	1672	Amide-I, β -turn
	1664	1663			1662		Amide-I, collagen
1650 & 1644			1645	1649		1644	Amide-I, random/ α -helix
1637	1637	1635		1619		1621	Amide-I, β -sheet
		1617		1606	1609		amino acids side chain (Glu, Arg), mainly from collagen
		1563		1568	1560	1559	Amide-II, collagen
				1557			Amide-II
1547	1548	1543	1546				Amide-II, α -helix
1521	1522	1517	1519	1524	1521	1514	Amide-II, β -sheets
1456	1456	1454	1452	1454	1453	1460	δ CH ₂
1404	1398	1402	1398	1401	1407	1405	vsCOO ⁻ (proteins)
	1342	1343	1343	1343	1341		Amide-III, collagen
1313	1313	1313	1313	1320	1314	1314	Amide-III
				1283			Amide-III
1236	1237	1236	1235	1253	1247		vaPO ₂ (nucleic acids, phospholipids)
1156	1161	1155	1161	1134	1180		vCO, vC-C, vC-O-C (polysaccharides)
1115	1108	1116	1105	1101			vCO, vC-C, vC-O-C (polysaccharides)
		1090			1093		vsPO ₂ , vPO ₄ (nucleic acids, phospholipids, hydroxyapatite from substrate)
1066	1068	1048	1073	1068	1064		vCO, vC-C, vC-O-C (polysaccharides)
1030	1029	1027	1033				vPO ₄ (hydroxyapatite from substrate)
				1024			vCO, vC-C, vC-O-C (polysaccharides)
				999	978		
961	960	960					vPO ₄ (hydroxyapatite from substrate)

Table 2:

A _a	A _b	A _c	B _d	B _e	B _f	Tentative assignment
1737	1739	1736	1742	1742	1743	vC=O (esters)
1689	1692	1696	1694	1691	1694	Amide-I, collagen
1676	1680 (sh)	1678	1678	1678	1679	Amide-I, β -turn
1658		1664	1662	1662	1662	Amide-I, collagen
	1650	1645	1646	1647	1646	Amide-I, random/ α -helix
	1634	1631 (sh)			1628	Amide-I, β -sheet
1623 (sh)	1614		1618	1628	1619	Amide-I, β -sheet
1611	1603	1606				Amino acids side chain (Glu, Arg), mainly from collagen
			1596	1597	1597	Amide-II
1579	1574	1578	1580	1573	1568	Amide-II, collagen
1548		1546	1548	1547	1548	Amide-II, α -helix
		1527		1526	1522	Amide-II, β -sheet
1513	1515	1511	1516	1514	1514	Amide-II, β -sheet
			1499	1499		
1451	1448	1458	1458	1460	1451	δ CH ₂
			1430	1430	1430	
		1407	1411	1411	1412	vsCOO ⁻
1393	1394		1392	1393	1393	vsCOO ⁻
1303		1373			1264	Amide-III
1247	1256		1257	1250		vaPO ₂ (nucleic acids, phospholipids)
				1227	1239	vaPO ₂ (nucleic acids, phospholipids)
1099			1104	1109		vCO, vC-C, vC-O-C (polysaccharides, nucleic acids)
1067	1079			1073		vCO, vC-C, vC-O-C (polysaccharides)
	1053	1051				vCO, vC-C, vC-O-C (polysaccharides)
982	985	980				vC-C, vP-O-P

Supplementary Material for publication

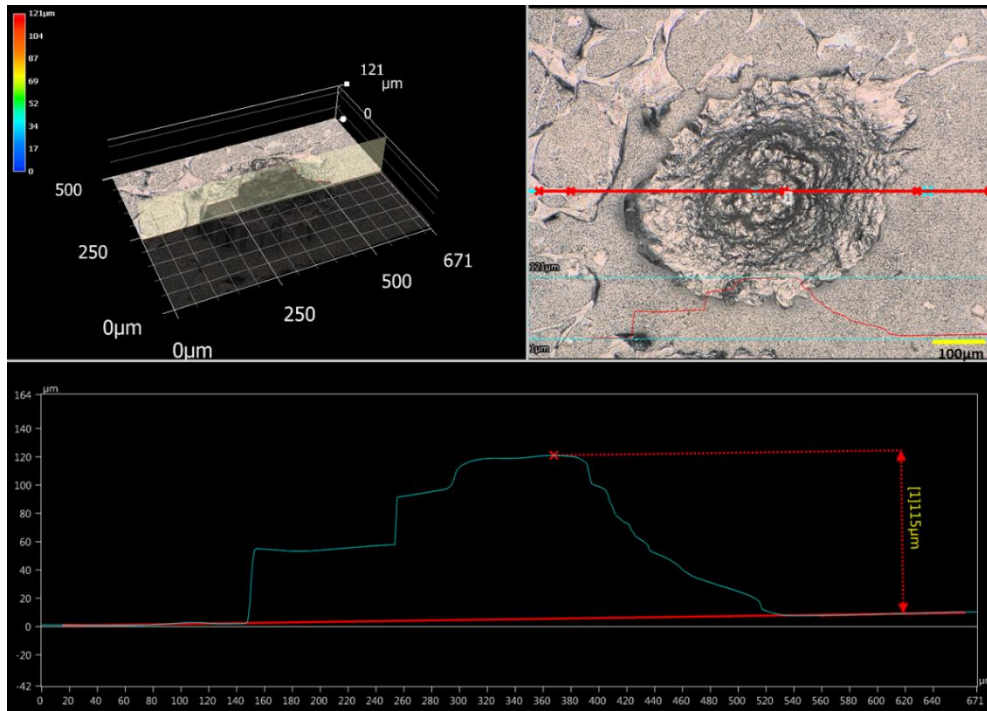


Figure SI-1: Digital microscopy footages (magnification $\times 500$, Objective ZS200) highlighting the bone-like nodule features including size and height. Scale bars: 100 μm .

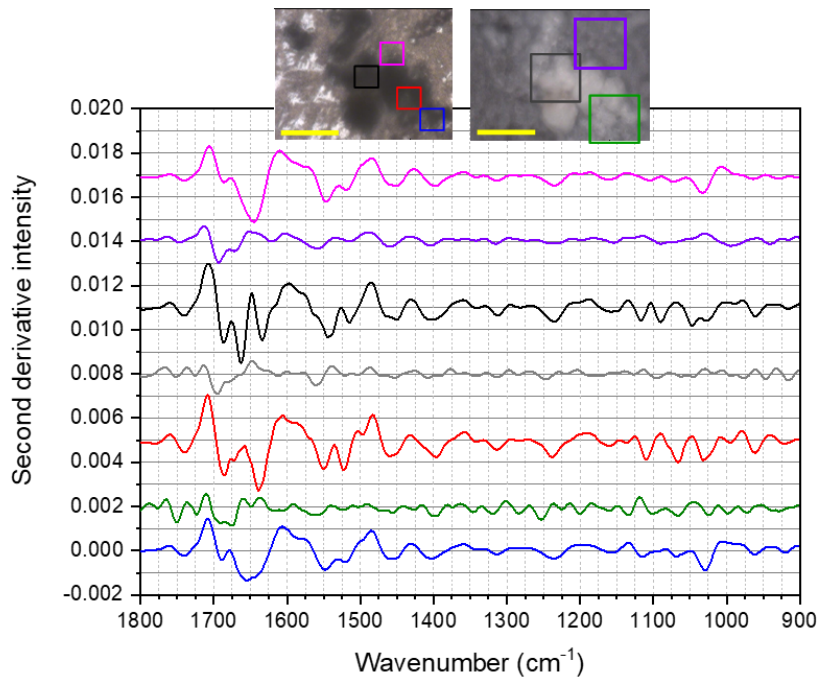


Figure SI-2: Micro-infrared second derivative spectra of a bone-like nodule grown for four weeks on ioM coated CaF_2 window in transmission (pink, black, red and blue squares and lines) and reflectance (violet, grey and green squares and lines) modes. Offsets of spectra are used for clarity. Images inserted: optical representation of the analyzed regions. Scale bars: 100 μm .

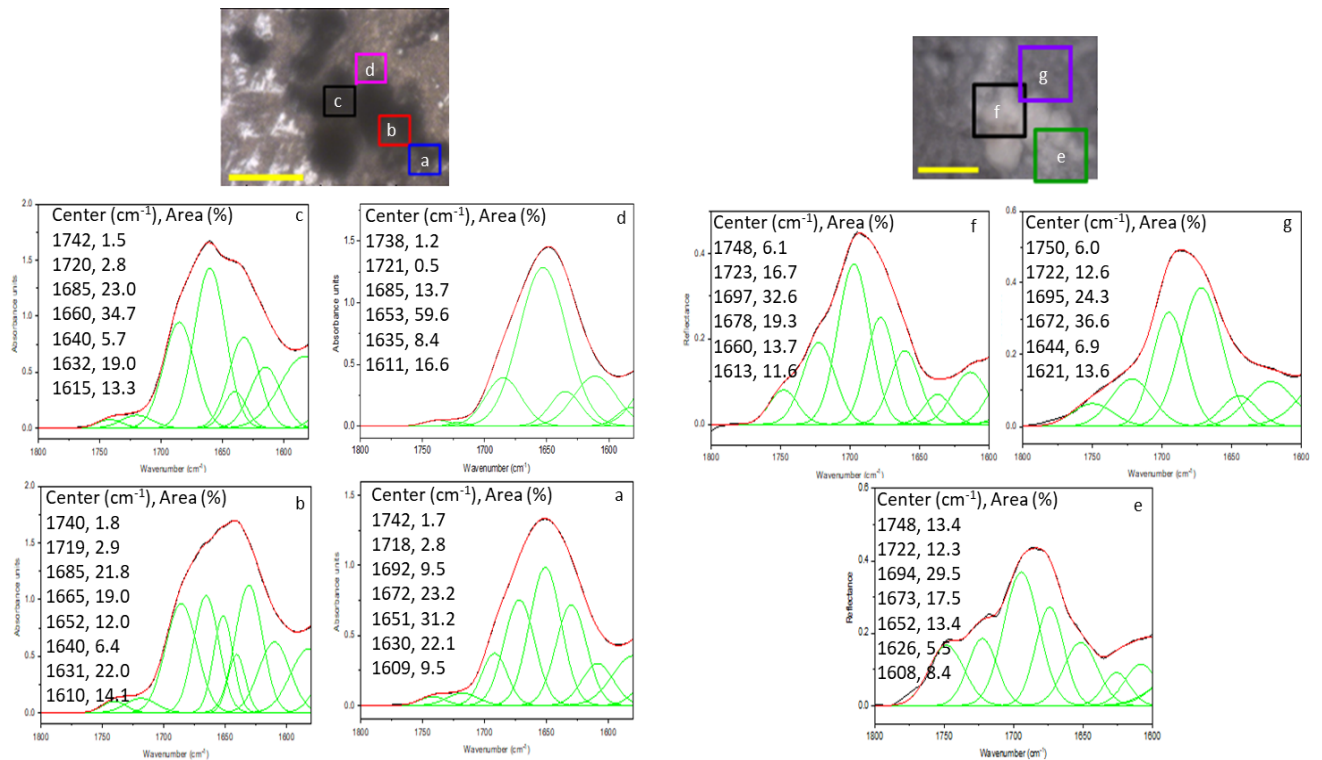


Figure SI-3: Curve fitting of the spectra in the amide I region for bone-like nodule grown for four weeks on ioM coated CaF₂ window in transmission (a, b, c, d) and in reflection (e, f, g) modes. Upper images: optical representation of the analyzed regions. Scale bars: 100 μm . The bands were determined using the second derivative spectra. A maximum of six bands were used for the fitting of amide I bands (region 1600-1700 cm^{-1}) and two bands for the C=O stretching's (above 1700 cm^{-1}).

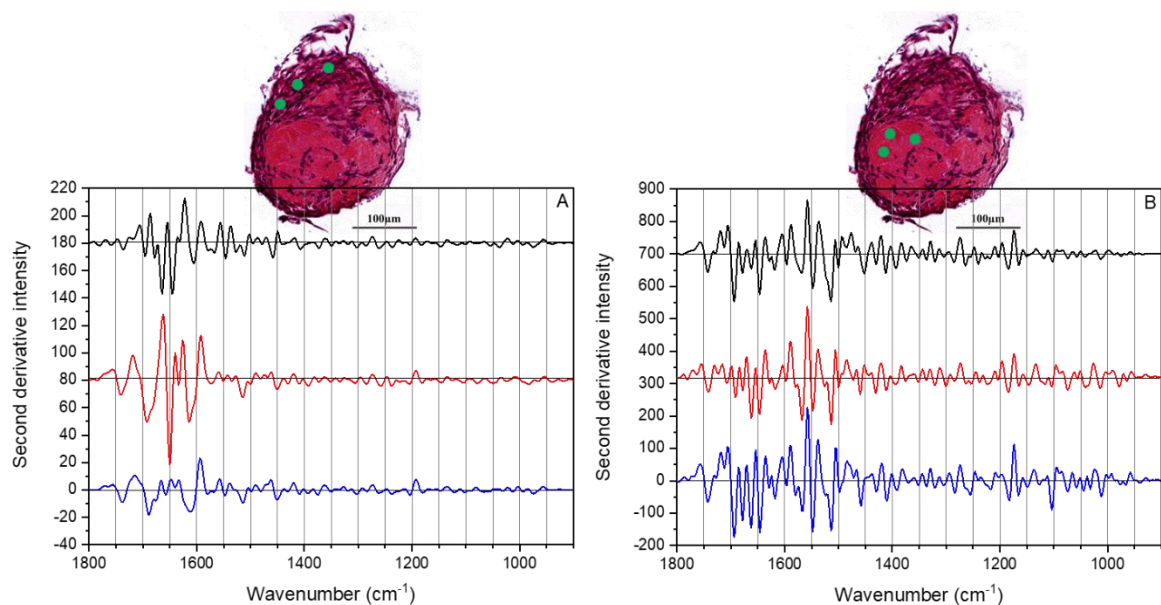


Figure SI-4: AFM-IR spectra second derivatives of a bone-like nodule grown for four weeks on ioM coated CaF₂ window and embedded in paraffin. A: cell-rich area. B: collagen-rich area. Inserts: optical representation of analyzed regions. Scale bars: 100 μm .

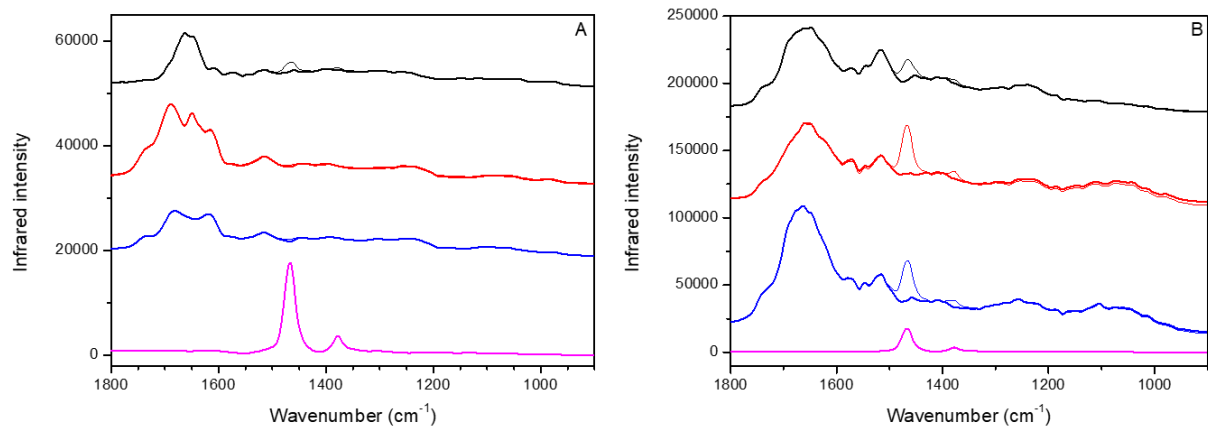


Figure SI-5: AFM-IR spectra before and after paraffin spectral subtraction. A: cell-rich region. B: collagen-rich region. Paraffin spectrum is also given at the bottom of each figure.

Videos captions

Video I: *Human stem cells behavior.* Time laps monitoring after 14 days of culture showing fibroblastic monolayer forming cells on glass substrate.

Video II: *Human stem cells behavior.* Time laps monitoring after 14 days of culture showing the formation, fusion and stabilization of bone-like nodules on IoM substrate.